A Novel Mechanism for Metal Alloying at the Nanoscale

by

Daiwei Yu

B. S. in Physics
Peking University, 2016

Submitted to the Department of Electrical Engineering and Computer Science
in Partial Fulfillment of the Requirements for the Degree of

Master of Science in Electrical Engineering and Computer Science

at the

MASSACHUSETTS INSTITUTE OF TECHNOLOGY

June 2018

© 2018 Massachusetts Institute of Technology. All rights reserved.

Signature of Author: Signature redacted
Department of Electrical Engineering and Computer Science
May 17, 2018

Certified by: Signature redacted
Ju Li
Battelle Energy Alliance Professor of Nuclear Science and Engineering
Professor of Materials Science and Engineering
Thesis Supervisor

Accepted by: Signature redacted
Leslie A. Kolodziejski
Professor of Electrical Engineering and Computer Science
Chair, Department Committee on Graduate Students

MITLibraries

77 Massachusetts Avenue
Cambridge, MA 02139
http://libraries.mit.edu/ask

DISCLAIMER NOTICE

Due to the condition of the original material, there are unavoidable flaws in this reproduction. We have made every effort possible to provide you with the best copy available.

Thank you.

The images contained in this document are of the best quality available.

A Novel Mechanism for Metal Alloying at the Nanoscale

by

Daiwei Yu

Submitted to the Department of Electrical Engineering and Computer Science on May 17, 2018
in Partial Fulfillment of the Requirements for the Degree of
Masters of Science in Electrical Engineering and Computer Science

Abstract

The controllable incorporation of multiple immiscible elements into a single nanoparticle merits untold scientific and technological potential, yet remains a challenge using conventional synthetic techniques. We propose a novel mechanism for metal alloying at the nanoscale, which provides a general route for alloying dissimilar elements into single-phase solid-solution nanoparticles, referred to as high-entropy-alloy nanoparticles (HEA-NPs). To validate the theory, we developed a facile carbothermal shock (CTS) method to synthesize a wide range of multicomponent (up to eight dissimilar elements) nanoparticles with a desired chemistry (composition), size, and phase (solid solution, phase-separated) by controlling the CTS parameters (substrate, temperature, shock duration, and heating/cooling rate). To prove utility, we synthesized quinary HEA-NPs as ammonia oxidation catalysts with ~100% conversion and >99% nitrogen oxide selectivity over prolonged operations. This mechanism is distinct from previously reported alloying processes, which can bring about a new repertoire of alloys and nanostructures with unprecedented functionalities.

Thesis Supervisor: Prof. Ju Li

Title: Battelle Energy Alliance Professor of Nuclear Science and Engineering & Professor of Materials Science and Engineering

Contents

Abstract 3

Contents 5

List of Figures 7

List of Tables 8

Chapter 1 Introduction 9

1.1 Motivation 9

1.2 Configurational entropy of mixing 10

1.3 Scope of the thesis work 11

Chapter 2 Experiment 13

2.1 Carbothermal shock method 14

2.2 Elemental characterization 17

2.3 Potential application 20

Chapter 3 Mechanism 23

3.1 Particle dispersion mechanism 23

3.1.1 Control experiments 23

3.1.2 Catalytically driven particle dispersion mechanism 26

3.2 Kinetics 31

3.2.1 Timescale analysis 31

3.2.2 Kinetic control over nanoparticle formation 32

Chapter 4 Conclusion 37

References 39

List of Figures

Fig. 1-1. Calculation of configurational entropy of mixing and simple classification of low, medium, and high entropy regions 11

Fig. 2-1. CTS synthesis of HEA-NPs on carbon supports 15

Fig. 2-2. SEM images of the decorated CNF microstructure before and after CTS 16

Fig. 2-3. Elemental characterization of HEA-NPs 18

Fig. 2-4. TEM images of 1-3 elements nanoparticles on CNFs with different loading concentrations 19

Fig. 2-5. Atomic percentage distributions for quinary nanoparticles by different synthesis methods 20

Fig. 2-6. Catalytic performance of quinary HEA-NPs (PtPdRhRuCe) for ammonia oxidation... 21

Fig. 2-7. Catalytic application of relatively inexpensive quinary HEA-NPs for ammonia oxidation 22

Fig. 3-1. Properties of CNF with different carbonization temperatures 24

Fig. 3-2. Particle dispersion mechanism for the CTS process 25

Fig. 3-3. In situ mass spectroscopy during the CTS process 27

Fig. 3-4. HEA-NPs on CNFs with and without CO_2 activation 30

Fig. 3-5. Ultrafine and well-dispersed quinary HEA-NPs (PtPdIrRhRu) formed on CA-CNFs.. 30

Fig. 3-6. Timescale for catalytically-driven particle fission/fusion 31

Fig. 3-7. Kinetic control over nanoparticle formation 33

Fig. 3-8. Defect concentrations of CNFs after various shock durations 34

Fig. 3-9. Rate-dependent non-equilibrium structures for both Cu-Co and Au-Ni systems 35

Fig. 3-10. Atomic HAADF images of AuNi synthesized with different cooling rates 35

Fig. 3-11. Synthesized nanoparticles by slow heating and cooling rates (control experiments).. 36

List of Tables

Table 2-1. Physi-chemical properties of the elemental precursor salts used and corresponding metals 13
Table 2-2. Miscibility between binary elemental combinations with a 1:1 ratio 16
Table 3-1. Physical properties of Au and Cu 25

Chapter 1

Introduction

1.1 Motivation

Multimetallic nanoparticles (MMNPs) are of interest in a wide range of applications, including catalysis (1–7), energy storage (8), and bio/plasmonic imaging (8, 9). Alloying multiple metallic elements into individual nanoscale products offers the promise of material properties that could exceed single element (or unary) nanoparticles (2, 5, 6). The current and primary approaches toward the preparation of MMNPs arise from wet-chemistry synthesis, where a variety of particle sizes, shapes, and phases can be attained (3, 4, 7, 10). However, most studies via wet-chemical methods report alloy compositions not exceeding three elements, which limits the compositional space. Additionally, more site-specific synthesis techniques, including printing- and lithography-based methods (1, 11, 12), have shifted the compositional space toward quaternary and even quinary nanostructures; however, the subsequent reduction procedures tend to limit the structural complexity to phase-separated MMNPs, especially for immiscible elemental combinations (1, 12, 13).

In terms of bulk material synthesis, melt processing is a scalable method that has led to the creation of high entropy alloys (HEAs) consisting of five or more elements in a solid solution (uniform mixing), which have shown great potential as structural materials (14–18). To date, only a limited family of HEAs have been achieved, due to the difficulty of mixing elements with vastly different chemical and physical properties, as well as cooling rate constraints. Moreover, downsizing HEAs to the nanoscale is a daunting task, especially by conventional alloying methods. Therefore, a new mechanism for metal alloying at the nanoscale is crucial to the development of a synthesis process where elemental composition, particle size, and phase can be precisely controlled.

1.2 Configurational entropy of mixing

The configurational entropy of mixing for multielement nanoparticles can be calculated according to following equation (Eq. 1-1) (16):

$$\Delta S_{mix} = -R \sum_{i=1}^{n} X_i ln X_i \qquad 1\text{-}1$$

where ΔS_{mix} is the configurational entropy of mixing, R is the gas constant, $\mathrm{X_i}$ is the molar ratio of component i, and n is the total number of elements involved. As shown in Fig. 1-1, the maximum mixing entropy (random mixing in an equal ratio) shows a well-defined sublinear relationship; as the amount of alloying elements increases, the mixing entropy ($\Delta \mathrm{S_{mix}}$) also increases in a logarithmic fashion: from low entropy ($\Delta \mathrm{S_{mix}} < 1\mathrm{R}$) for unary and binary alloys, to medium entropy ($1\mathrm{R} < \Delta \mathrm{S_{mix}} < 1.5\mathrm{R}$) for ternary and quaternary alloys, and high entropy alloys ($\Delta \mathrm{S_{mix}} > 1.5\mathrm{R}$), according to the classifications in high entropy alloys research (16). The majority of conventionally synthesized nanoparticles are composed of a limited number of elements and thus, fall into the category of low entropy alloys. The top-down assembly processes (dip-pen lithography) can mechanically confine nanoparticles composed of 5 elements, however phase separation occurs within the MMNPs which drastically decreases their mixing entropy. By utilizing the CTS process mentioned below, multimetallic mixing of numerous elements (up to 8) can be readily achieved, pushing the synthesis capabilities towards the high entropy region. Note that the term "high entropy alloy nanoparticles" (HEA-NPs) in this work denotes solid solution structures since the high entropy mixing liquid metal state is retained by rapid quenching. Thus, our definition of HEA-NPs is not directly dependent on the number of elemental constituents.

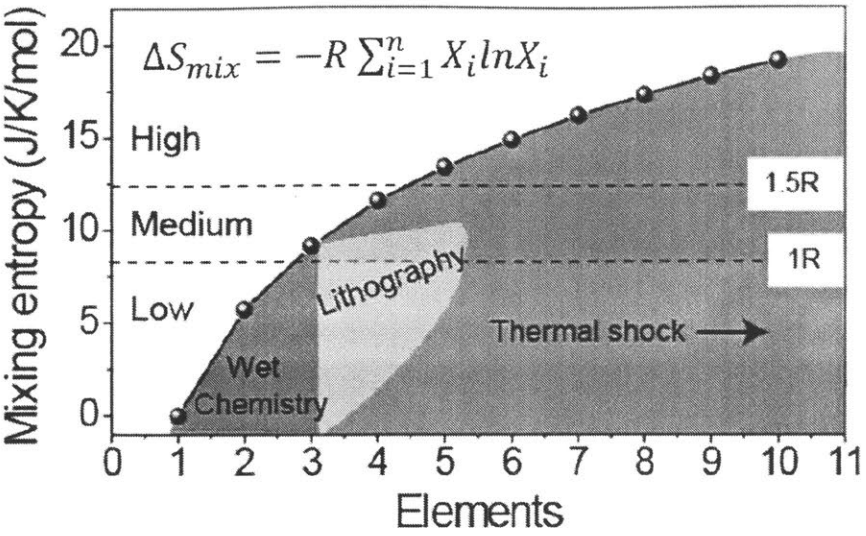

Fig. 1-1. Calculation of configurational entropy of mixing and simple classification of low, medium, and high entropy regions (16). MMNPs synthesized by different methods fall into different entropy regions (based on the classical definition of high entropy alloys).

1.3 Scope of the thesis work

While the thesis work mainly focuses on the mechanism study, specific experiments have also been designed to validate and perfect the theory. In order to better elucidate the mechanism, this thesis starts with a brief introduction of experiments together with some discussions of the key results in chapter two. Then detailed mechanism analysis is illustrated in chapter three, including both thermodynamics and kinetics. The last chapter summarizes the thesis work with conclusions and remarks, as well as its scientific and technological potential.

Chapter 2

Experiment

As mentioned before, conventional wet-chemical methods typically produce nanoparticles limited to only three different elements, and recent site-specific synthesis techniques can only make phase-separated multimetallic nanoparticles after reduction procedures. In order to synthesize high-entropy-alloy nanoparticles (HEA-NPs), we think maybe using a physical science approach is better than any traditional chemistry approach. Also fast kinetics is crucial to maximize the mixing entropy, which is hard to be achieved by conventional slow chemical reduction procedures. Fortunately it turns out that carbothermal shock (CTS) is such an ideal method that precise control over different parameters (temperature, duration, and ramp rate) during the synthesis process is quite easy. Based on our theory, we select ideal material support (oxygenated carbon) and employ flash heating and cooling (temperature of ~2000 K, shock duration of ~55 ms, and ramp rates on the order of 10^5 K/s) to successfully produce HEA-NPs with up to eight dissimilar metallic elements (Table 2-1) for the first time.

Table 2-1. Physi-chemical properties of the elemental precursor salts used and corresponding metals.

Precursors	Chemical reduction potential [V]	Physcical decomposition T [K]	Metals	Atomic Radius [Å]	Melting point [K]	Boiling point [K]	Room-T structure
H_2PtCl_6	0.68, 0.73, 1.18	573, 653, 853	Pt	1.39	2041	4098	FCC
$PdCl_2$	0.95	952	Pd	1.37	1828	3236	FCC
$NiCl_3$	-0.25	>1073	Ni	1.24	1728	3186	FCC
$FeCl_3$	0.77, -0.44	553, 588	Fe	1.26	1811	3134	BCC
$CoCl_2$	-0.28	>873	Co	1.25	1768	3200	HCP
$HAuCl_4$	1.5	527	Au	1.44	1337	3129	FCC
$CuCl_2$	0.34	1266	Cu	1.28	1358	3200	FCC
$SnCl_2$	-0.14	896	Sn	1.40	505	2875	Tetragonal

Reduction potential relative to standard hydrogen electrode;
FCC: face-centered-cubic; BCC: body-centered-cubic; HCP: hexagonal-close-packing.

2.1 Carbothermal shock method

The CTS method we used to synthesize uniformly dispersed, solid-solution nanoparticles (up to eight elements) requires two steps. First, we mixed metal salt precursors MCl_xH_y (M is Pt, Pd, Ni, Fe, Co, Au, Cu, or Sn, among others) into a solution and loaded onto a conductive carbon support, such as carbon nanofibers (CNFs). CNFs carbonized at 1073 K (CNF-1073K, denoted as CNF hereafter) are the substrates used in this work unless stated otherwise. After drying, we exposed the precursor-loaded sample to a rapid thermal shock (55 ms) in an Ar-filled glovebox, which leads to a high concentration of nanoparticles (e.g., PtNi) that form across the carbon surface (Fig. 2-1a and Fig. 2-2). The electrical pulse that we applied controls the thermal exposure conditions (Fig. 2-1b), with a common temperature of ~2000 K and heating/cooling rates up to ~10^5 K/s as measured with a pyrometer. We found no apparent elemental segregation or phase separation for the PtNi nanoparticles (Fig. 2-1c) using scanning transmission electron microscopy (STEM) elemental maps. The high-angle annular dark-field (HAADF) images and atomic maps also demonstrated both uniform atomic scale mixing and the formation of a face-centered cubic (fcc) crystalline structure (Fig. 2-1c). Our general method extends to more complex HEA-NPs. For example, we readily fabricated HEA-NPs composed of eight dissimilar elements (Pt, Pd,Ni, Co, Fe, Au, Cu, and Sn). These elements have a range of atomic radii (1.24 to 1.44 Å), reduction potentials (-0.25 to 1.5 V versus the standard hydrogen electrode), preferred crystal structures (face-centered cubic, body-centered cubic, hexagonal close-packed, or tetragonal), and melting temperatures (500 to 2000 K) that typically prevents solid-solution formation (Fig. 2-1d and Table 2-2).

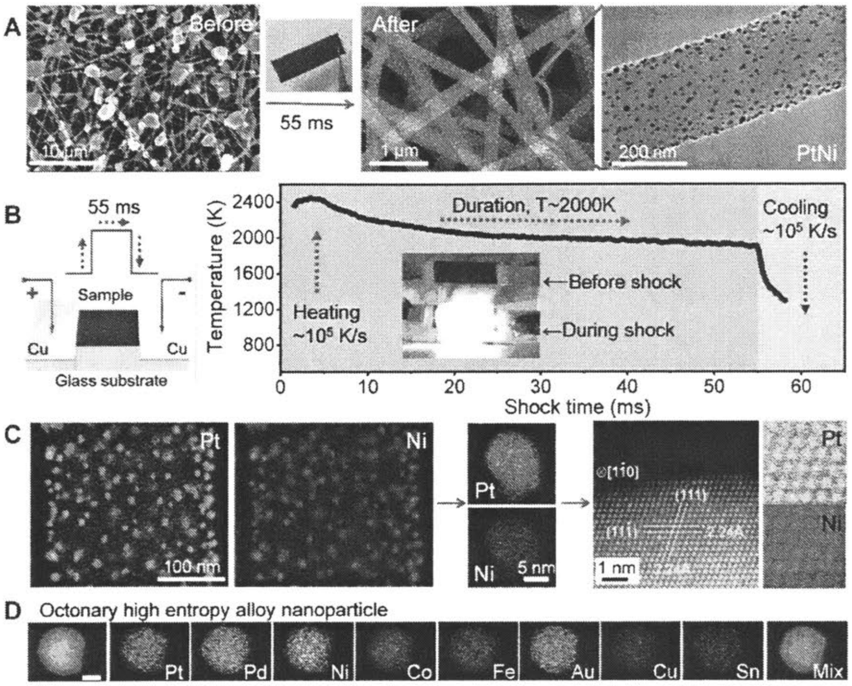

Fig. 2-1. CTS synthesis of HEA-NPs on carbon supports. (a) Microscopy images of microsized precursor salt particles on the carbon nanofiber (CNF) support before thermal shock, as well as the synthesized, well-dispersed (PtNi) nanoparticles after CTS. (b) Sample preparation and the temporal evolution of temperature during the 55 ms thermal shock. (c) Low-magnification and single-particle elemental maps, an HAADF image, and corresponding atomic maps for a binary PtNi alloy. (d) Elemental maps of an HEA-NP composed of eight dissimilar elements (Pt, Pd, Ni, Co, Fe, Au, Cu, and Sn). Scale bar, 10 nm.

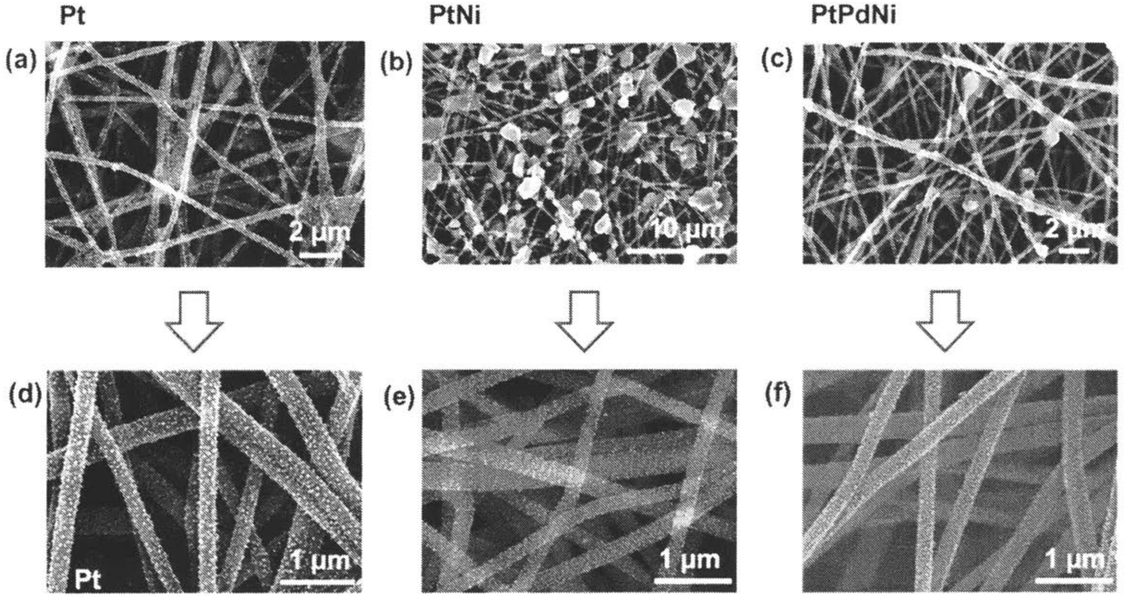

Fig. 2-2. SEM images of the decorated CNF microstructure before and after CTS. (a) Pt, (b) PtNi, and (c) PtPdNi precursors on CNFs before CTS as well as the synthesized (d) Pt, (e) PtNi, and (f) PtPdNi nanoparticles after CTS.

Table 2-2. Miscibility between binary elemental combinations with a 1:1 ratio.

[Data from ASM Alloy Phase Diagram Database]

	Pt	Pd	Co	Ni	Fe	Au	Cu	Sn
Pt	1	0	1	1	1	1	1	0
Pd	0	1	1	1	0	1	1	1
Co	1	1	1	1	0	0	0	0
Ni	1	1	1	1	0	0	0	0
Fe	1	0	0	0	1	0	0	0
Au	1	1	0	0	0	1	1	0
Cu	1	1	0	0	0	1	1	0
Sn	0	1	0	0	0	0	0	1

Note: 1 forms an alloy or intermetallic; 0 are immiscible

2.2 Elemental characterization

Conventional reduction procedures (1, 3) tend to create phase-separated heterostructures among immiscible elements, which greatly reduces the configurational entropy of mixing (Fig. 1-1). The CTS process leads to solid solution MMNPs (i.e., HEA-NPs), where arbitrary metallic elements are completely mixed to maximize the mixing entropy (ΔS_{mix}) (Fig. 2-3a). We demonstrated the versatility by synthesizing a series of multielement nanoparticles and characterized them by STEM, transmission EM (TEM), scanning EM (SEM), and energy-dispersive x-ray spectroscopy (EDS). We synthesized unary (Pt, Au, and Fe), binary (PtNi, AuCu, and FeNi), and ternary (PtPdNi, AuCuSn, and FeCoNi) nanoparticles that exhibit compositional uniformity (Fig. 2-3b). The nanoparticles also possess size uniformity, with diameters of $\geqslant 5$ nm (Fig. 2-4), regardless of the elemental compositions. By adding additional metal salts to the precursor solutions, we synthesized quinary (PtCoNiFeCu and PtPdCoNiFe), senary (PtCoNiFeCuAu), septenary (PtPdCoNiFeCuAu) and octonary (PtPdCoNiFeCuAuSn) HEA-NPs, which are solid solutions and evenly dispersed across the carbon support (Fig. 2-3c and d). Moreover, the HEA-NPs are of nanoscale dimensions in fcc crystal structures (Fig. 2-3d).

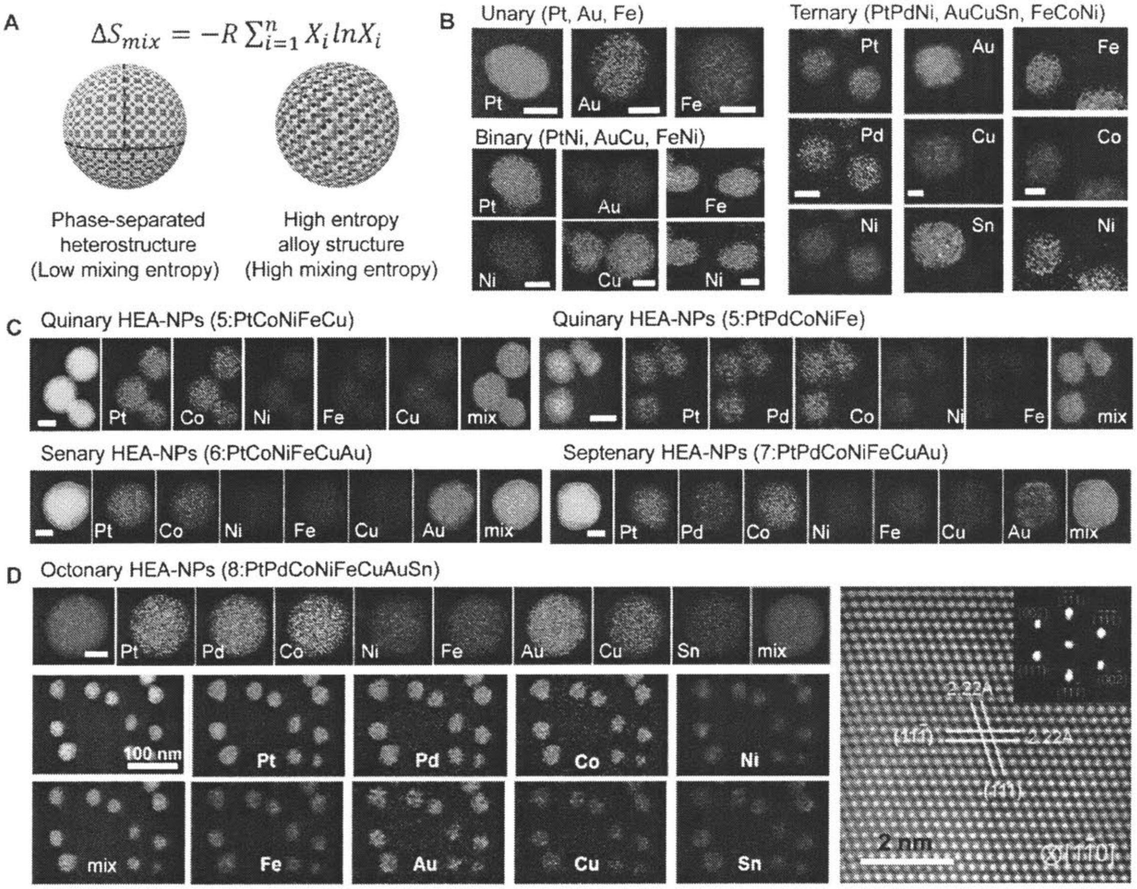
A
$\Delta S_{mix} = -R\sum_{i=1}^{n} X_i ln X_i$
Phase-separated heterostructure (Low mixing entropy)
High entropy alloy structure (High mixing entropy)
B
Unary (Pt, Au, Fe)
Pt
Au
Fe
Binary (PtNi, AuCu, FeNi)
Pt
Au
Fe
Ni
Cu
Ni
Ternary (PtPdNi, AuCuSn, FeCoNi)
Pt
Au
Fe
Pd
Cu
Co
Ni
Sn
Ni
C
Quinary HEA-NPs (5:PtCoNiFeCu)
Pt
Co
Ni
Fe
Cu
mix
Quinary HEA-NPs (5:PtPdCoNiFe)
Pt
Pd
Co
Ni
Fe
mix
Senary HEA-NPs (6:PtCoNiFeCuAu)
Pt
Co
Ni
Fe
Cu
Au
mix
Septenary HEA-NPs (7:PtPdCoNiFeCuAu)
Pt
Pd
Co
Ni
Fe
Cu
Au
mix
D
Octonary HEA-NPs (8:PtPdCoNiFeCuAuSn)
Pt
Pd
Co
Ni
Fe
Au
Cu
Sn
mix
100 nm
Pt
Pd
Co
Ni
mix
Fe
Au
Cu
Sn
2.22Å
2.22Å
2 nm
[110]

Fig. 2-3. Elemental characterization of HEA-NPs. (a) Schematic comparison of phase-separated heterostructures synthesized by a conventional slow reduction procedure (slow kinetics) versus solid-solution HEA-NPs synthesized by the CTS method (fast kinetics). (b) STEM elemental maps of unary (Pt, Au, and Fe), binary (PtNi, AuCu, and FeNi), and ternary (PtPdNi, AuCuSn, and FeCoNi) nanoalloys. Scale bar, 5 nm. (c) HAADF images and STEM elemental maps of HEA-NPs: quinary (PtFeCoNiCu and PtPdCoNiFe), senary (PtCoNiFeCuAu), and septenary (PtPdCoNiFeCuAu). Scale bar, 10 nm. (d) Individual and low-magnification elemental maps (left) and a high-resolution HAADF-STEM image with fast Fourier transform analysis (right) of octonary (PtPdCoNiFeCuAuSn) HEA-NPs, showing solid solutions with an fcc structure. The low-magnification elemental maps verify the structural and compositional uniformity of the HEA-NPs. Scale bar, 10 nm.

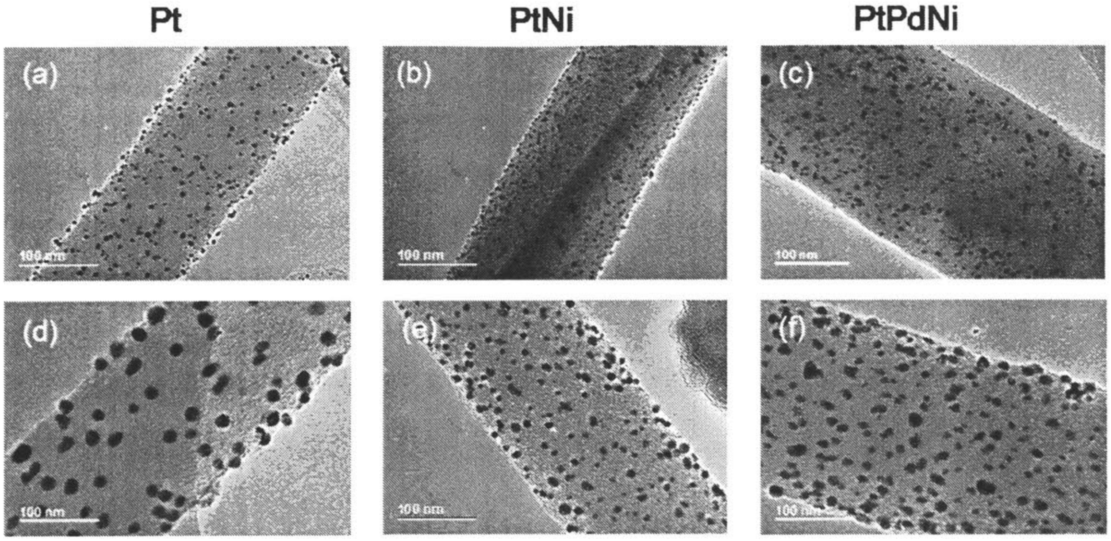

Fig. 2-4. TEM images of 1-3 elements nanoparticles on CNFs with different loading concentrations. Pt, PtNi, and PtPdNi with a precursor concentration of (a-c) 0.01 mol/L and (d-f) 0.05 mol/L per composition, respectively.

The HEA-NPs exhibited solid solution mixing via the same 55 ms thermal shock protocol. We confirmed the structural uniformity (no phase separation) and negligible chlorine content with STEM, x-ray diffraction (XRD), and x-ray photoelectron spectroscopy (XPS). A statistical study conducted over different sample regions confirms the compositional uniformity among the synthesized nanoparticles. For example, the compositional variation for each element in our quinary HEANPs (PtPdCoNiFe) is ~10%, which is smaller than the >50% variation reported for lithography based techniques (Fig. 2-5) (1). Additionally, the macroscopic compositions that we determined by inductively coupled plasma mass spectroscopy (ICP-MS) agree well with the STEM-derived statistics. The HEA-NP composition has a small deviation from the ideal composition based on the initial precursor salt molar ratios, due to vapor loss at high temperature. To demonstrate compositional control, we employed the (precursor) compensation approach, which is a common strategy in high-temperature synthesis when volatile elements are involved.

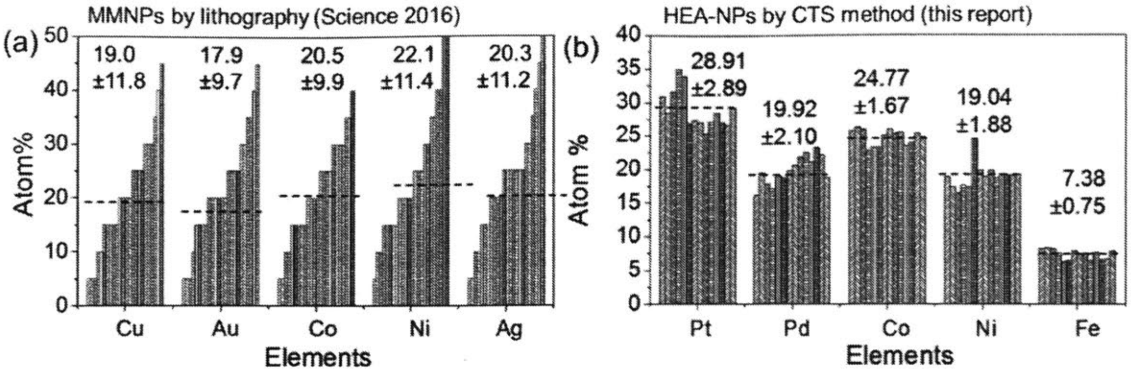

Fig. 2-5. Atomic percentage distributions for quinary nanoparticles by different synthesis methods. (a) Quinary MMNPs synthesized by scanning probe copolymer lithography (1). (b) Quinary HEA-NPs synthesized by our CTS method. A more uniform elemental/compositional distribution is achieved using our CTS method.

2.3 Potential application

The CTS method enables diverse compositions of uniformly mixed HEA-NPs that have potential for a wide range of applications. As a proof of concept, we demonstrated quinary HEA-NPs as advanced catalysts for ammonia oxidation, which is the key processing step in the industrial synthesis of nitric acid (Fig. 2-6a) (32). Despite extensive efforts on the exploration of new catalysts, PtPdRh-based multimetallic catalysts are still widely employed in industry to this day (33). Beyond the high content of precious metals, these catalysts also require very high temperatures (>800°C) to achieve high yields of NO_x ($NO + NO_2$) versus N_2/N_2O and tend to degrade under continuous operation (34). Using the CTS method, quinary PtPdRhRuCe HEA-NPs were prepared and employed as ammonia oxidation catalysts (21). We introduced Ru and Ce to improve the overall catalytic activity and reduce the Pt content (35, 36).

We achieved ~100% conversion of ammonia (NH_3) and >99% selectivity toward NO_x ($NO + NO_2$) at a relatively low operation temperature of 700°C with the PtPdRhRuCe HEA-NP catalyst (Fig. 2-6b). For comparison, we prepared similar catalysts (in terms of composition) by the wet impregnation method (denoted as PtPdRhRuCe MMNPs), which produced a 18.7% yield of NO_x at the same operation temperature, whereas most of the output was N_2 (Fig. 2-6c). An elemental map comparison between the two catalysts suggests that the enhanced catalytic selectivity of the HEA-NPs is likely due to the highly homogeneous nature of the solid-solution nanoparticles compared with the phase-separated heterostructures derived from the wet impregnation method (Fig. 2-6d). Note that synthesizing solid-solution PtPdRh multimetallic systems by conventional synthetic methods is challenging due to immiscibility (2, 34). We also performed degradation testing to study catalytic performance under prolonged operation conditions, and we observe no degradation in terms of catalytic activity or selectivity over ~30 hours of continuous operation at 700°C (Fig. 2-6e). We attributed this durability to the high-entropy nature of the catalysts prepared by the CTS method, which helps stabilize the MMNPs in solid solutions (i.e., HEA-NPs) and prevents phase separation or elemental segregation under the reaction conditions (16, 18). Moreover, the precious metal content of the HEA-NPs can be reduced further without compromising catalytic performance or stability by replacing ~37.5% of Pt with Co and eliminating Ru (e.g., PtPdRhCoCe HEA-NPs) (Fig. 2-7). Thus, HEA-NPs fabricated by the CTS method may be a general route toward highly active, durable, and cost-effective catalysts.

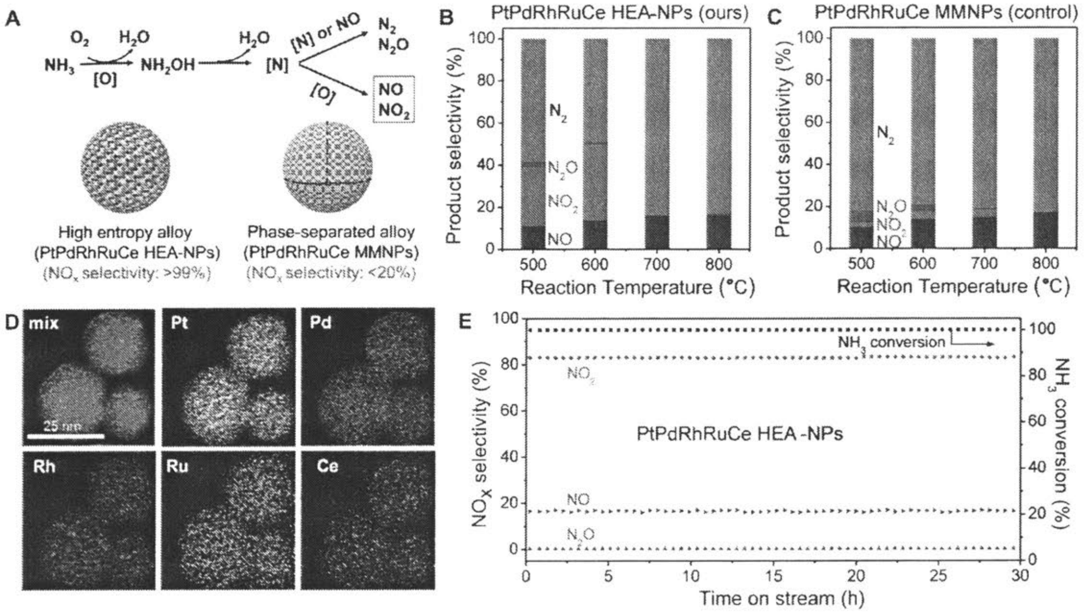

Fig. 2-6. Catalytic performance of quinary HEA-NPs (PtPdRhRuCe) for ammonia oxidation. (a) Reaction scheme for the ammonia oxidation process as well as the structural and performance differences between the PtPdRhRuCe HEA-NPs synthesized by CTS and the control sample (PtPdRhRuCe MMNPs) by wet impregnation. (b and c) Temperature-dependent product distribution and conversion of NH_3 for

PtPdRhRuCe HEA-NPs and PtPdRhRuCe MMNPs, respectively. (d) STEM elemental maps for PtPdRhRuCe HEA-NPs. (e) The time-dependent catalytic performance of PtPdRhRuCe HEA-NPs at 700°C.

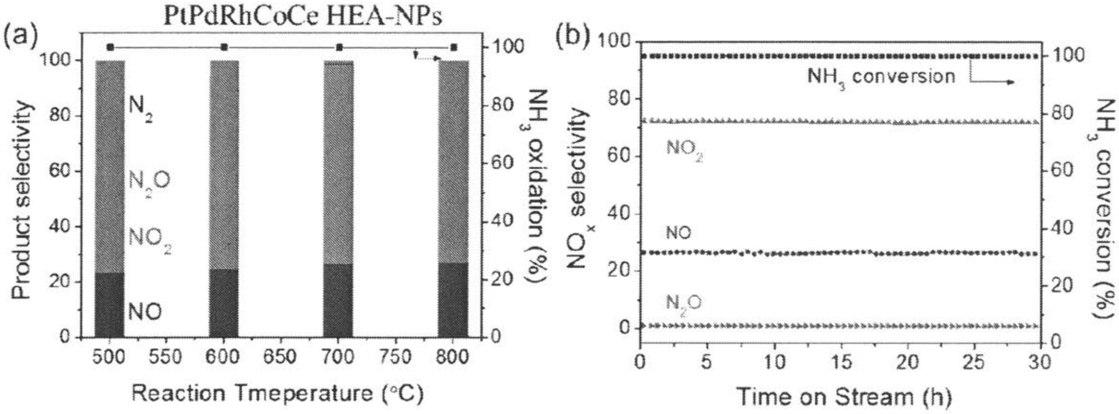

Fig. 2-7. Catalytic application of relatively inexpensive quinary HEA-NPs for ammonia oxidation. (a) Temperature-dependent product distribution (left) and conversion (right) of NH_3 oxidation for the PtPdRhCoCe HEA-NP sample; (b) time-dependent catalytic performance of PtPdRhCoCe HEA-NPs at 700°C.

Chapter 3

Mechanism

The HEA-NPs deviate from the phase-separated thermodynamic equilibrium structures reported in literature (1, 3, 12) due to the rapid quench induced nucleation/growth process of the CTS method, which "freezes" the liquid alloy state to create solid-solution nanoparticles. And that's the main reason why we thought CTS would be an ideal method to achieve our goals.

However, except for the nonequilibrium process we expected, the morphologies of the synthesized nanoparticles indicate a formation mechanism for CTS that further differs from other alloying approaches. Because ~2000 K far exceeds the thermal decomposition temperature of metal precursors (Table 1-1), the salts easily decompose (Eq. 3-1):

$$MCl_xH_y \rightarrow M(liq) + gases \uparrow \tag{3-1}$$

However, ~2000 K is below the boiling points of the metallic elements. In this case, the metallic elements are likely in the liquid phase and should be on a similar length scale as the initial (microsized) salt precursors. Since metals are nonwetting with carbon, the liquid metals should coarsen to minimize their surface energy at high temperature (22). Our observation departs from this behavior, so we designed some control experiments to refine the mechanism, and finally came up with a complete theory to explain how initially single-element, micron-sized liquid metal droplets can form uniformly dispersed alloy nanoparticles.

3.1 Particle dispersion mechanism

3.1.1 Control experiments

We performed two control experiments to explore HEA-NP formation mechanism. We first hypothesized that the defect concentration is the fundamental reason for the effective dispersal of metallic nanoparticles on the carbon support. To verify this, control experiments were conducted using synthesized nanoparticles on CNFs with different degrees of crystallinity. The low temperature carbonized CNFs (CNF-873K and CNF-1073K) have more defects than CNFs carbonized at high temperature (CNF-1273K) (Fig. 3-1). Each pyrolysis temperature was insufficient to drive away all surface-bound oxygen (O*) and thus resulted in an increasing amount of O* residuals remaining on CNFs carbonized at lower temperatures. As shown in Fig. 3-2a, increasing the carbonization temperature causes the synthesized nanoparticles to become larger and less uniform in terms of dispersion. This result confirms that defects enable uniform dispersions on CNFs. For substrates lacking defects, the particles can only coarsen without forming fine nanoparticles.

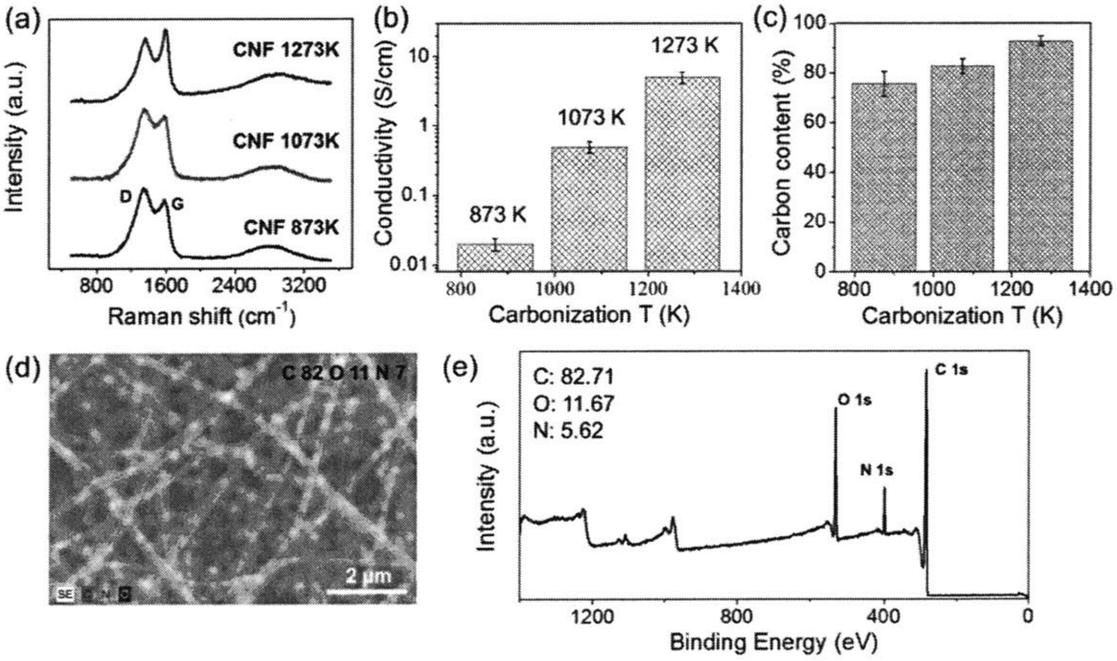

Fig. 3-1. Properties of CNF with different carbonization temperatures. (a) Raman spectra and (b) conductivity of CNF films carbonized at different temperatures: 873 K, 1073 K, and 1273 K. (c) Carbon content in CNFs carbonized at different temperatures, identified by point maps via SEM. (d) Elemental map of the carbon, nitrogen, and oxygen and (e) XPS profile of CNF carbonized at 1073 K.

Our second control experiment used identical CNF supports (CNF-1073K) and synthesis conditions (55 ms, ~2000 K), but with a variety of single metal salt precursors (Fig. 3-2b). Nanoparticle size distribution changes in this case with Cu having a much larger particle size

(~56.8 nm) than Au (~13.5 nm) and Pt (~6.3 nm). This trend resembles the catalytic activities of the corresponding elements, with Pt and Cu being the most and least active, respectively (21). Because Au and Cu possess similar physical properties (Table 3-1), the discrepancy requires a different particle dispersion mechanism than a simple, physical melting-and-nucleation process.

Table 3-1. Physical properties of Au and Cu.

Metals	Atomic Radius [Å]	Melting point [K]	Boiling point [K]	Room-T structure	Wetting angle at ~1330K
Au	1.44	1337	3129	FCC	138°
Cu	1.28	1358	3200	FCC	139°

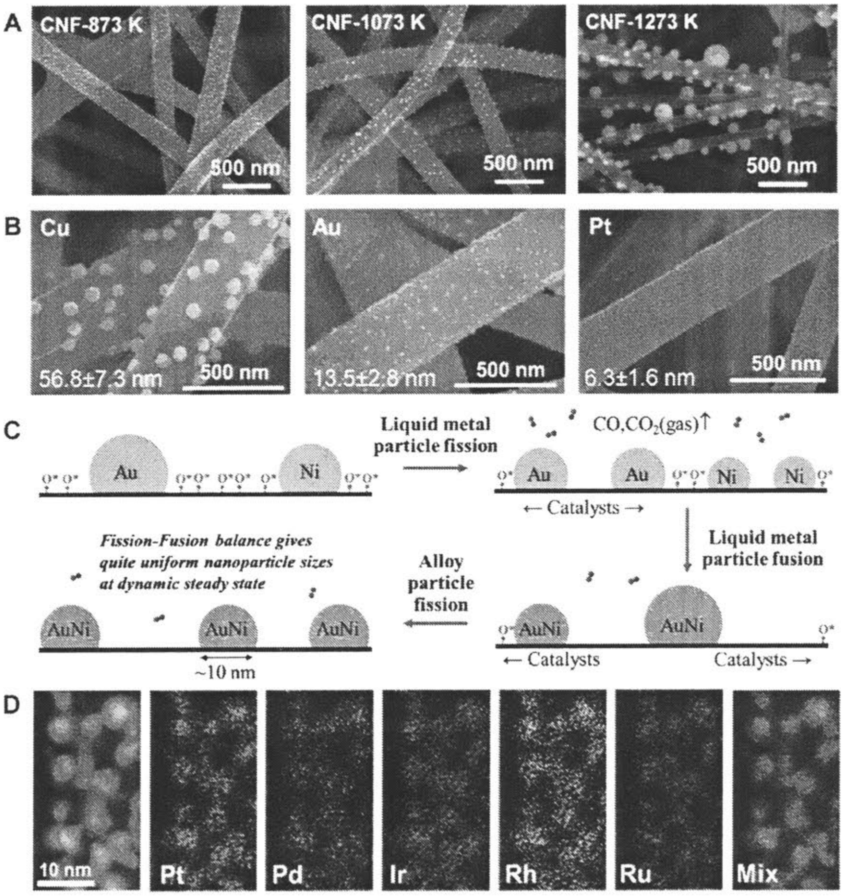
A
CNF-873 K
500 nm
CNF-1073 K
500 nm
CNF-1273 K
500 nm
B
Cu
56.8±7.3 nm
500 nm
Au
13.5±2.8 nm
500 nm
Pt
6.3±1.6 nm
500 nm
C
O* O*
Au
O* O* O* O* O*
Ni
O* O*
Liquid metal particle fission
CO,CO₂(gas)↑
O* Au
Au
O* O* Ni
Ni O*
← Catalysts →
Liquid metal particle fusion
Fission-Fusion balance gives quite uniform nanoparticle sizes at dynamic steady state
AuNi
AuNi
AuNi
~10 nm
Alloy particle fission
O* AuNi
AuNi
O*
← Catalysts
Catalysts →
D
10 nm
Pt
Pd
Ir
Rh
Ru
Mix

Fig. 3-2. Particle dispersion mechanism for the CTS process. (a) SEM images of synthesized AuNi nanoparticles on CNFs carbonized at different temperatures: 873, 1073, and 1273 K. A higher carbonization temperature leads to higher crystallinity and lower defect concentrations within the carbon support, which

affects particle size and dispersion. (b) SEM images of Cu, Au, and Pt particle distributions synthesized on identical CNF supports via the same CTS process. The higher catalytic activities of the metal species (Au and Pt) lead to smaller nanoparticles and more uniform distributions. (c) An illustration of the catalysis-driven particle fission/fusion mechanism to synthesize uniformly dispersed HEA-NPs. (d) HAADF image and elemental maps of ultrafine and well-dispersed quinary HEA-NPs (PtPdIrRhRu) on CO_2-activated CNFs. A narrow size distribution is achieved by increasing the support's surface defect concentration through CO_2 activation, as well as employing metal species with high catalytic activities.

3.1.2 Catalytically driven particle dispersion mechanism

Since defects and metal catalysts play a key role during the CTS process, we considered a catalytically driven particle dispersion mechanism for the defective carbon supports. To verify this, we used in situ mass spectrometry to analyze the gases created during CTS for defective CNF supports with and without precursor salts. Compared with bare CNF, the precursor-loaded CNF exhibited a larger and much sharper release of CO gas during the CTS process (Fig. 3-3). Thus, the release of CO gas upon thermal shock arises from a catalytically driven carbon metabolism reaction (Eq. 3-2):

$$C + O^{*} \rightarrow CO \uparrow \qquad \text{3-2}$$

where O* denotes surface-bound residual oxygen. The carbon metabolism reaction involves C (fuel), O* (oxidizer), and metal (catalyst), which correlates the surface defect concentration (e.g., carbonization temperature) and the metal's catalytic activity to the final nanoparticle size and level of dispersity. We hypothesize that during the 55 ms high-temperature exposure, the liquid metal droplets actively travel around and split ("fission") to harvest the dispersed O* on the carbon surface based on the catalytically driven reaction, C + O* = CO (gas) ($\Delta H = -110.5$ kJ/mol). Previously published works (23–26) and an in situ TEM study (27) also showed that metallic particles can move and split under a catalytic driving force, which is similar to our proposed carbon metabolism reaction.

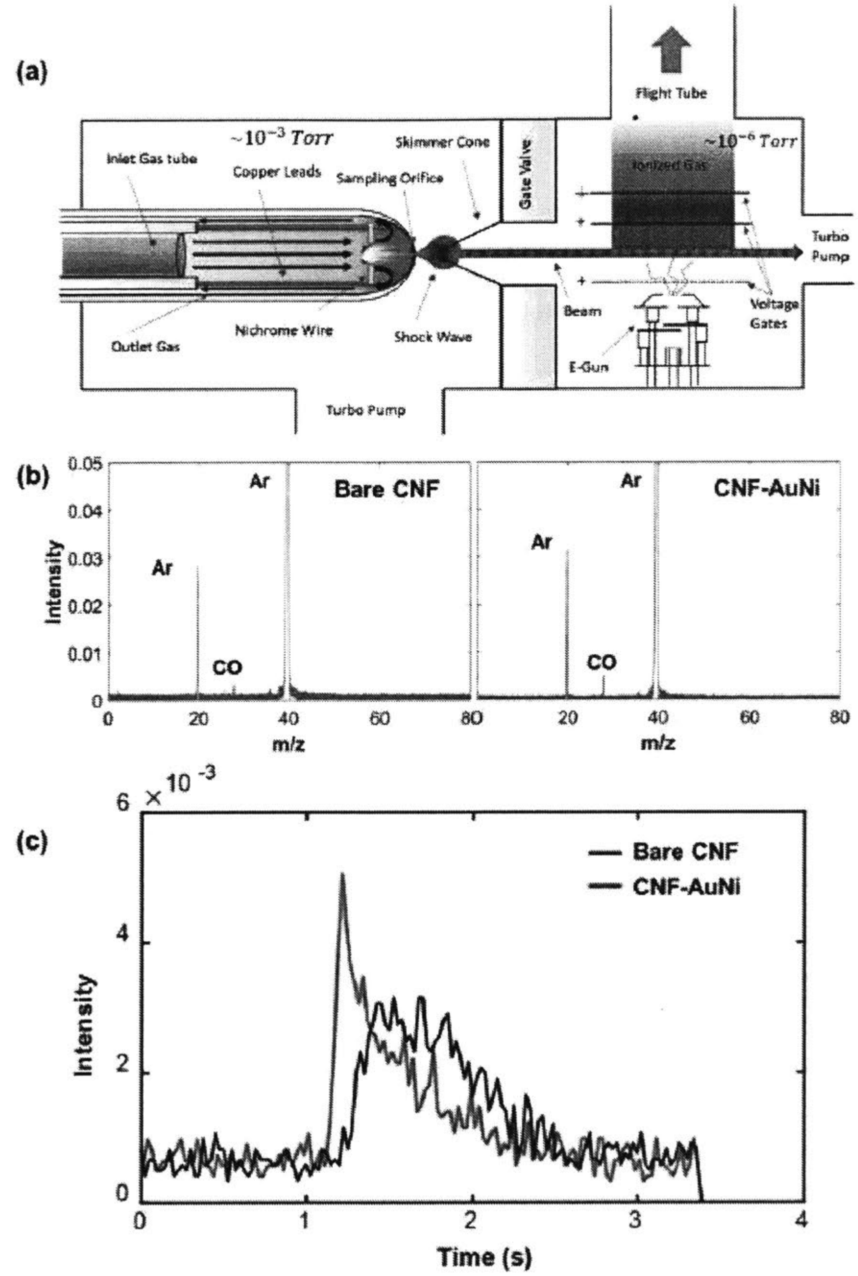

Fig. 3-3. In situ mass spectroscopy during the CTS process. (a) Experimental setup and Molecular Beam Mass Spectrometer schematic for flame sampling during combustion. (b) The full mass spectrum obtained during a 55 ms high temperature CTS for bare CNF and CNF-AuNi. (c) Temporal CO emission profiles for bare CNF and CNF-AuNi. The CNF-AuNi sample shows a sharp peak in terms of CO release compared to bare CNF, which demonstrates a catalytic carbon metabolism (C+O*=CO↑) reaction occurs during the CTS process.

Mechanistically (Fig. 3-2c), we proposed the catalytic metabolism-induced "particle fission and fusion" mechanism as the origin for the uniform dispersion of nanoparticles on oxygenated carbon by the CTS method. Here, particle fusion means several particles meet and coalesce into one particle, while particle fission refers to one particle splitting into several smaller particles. Briefly, the high temperature provides energy for particles to move around and undergo fusion, while the catalytic metabolism [$C + O^* = CO$ (gas)] provides the driving force for particle fission/splitting; the numerous particle fission/fusion events yield a dynamic steady state, where uniformly distributed nanoparticles form on the carbon surface after rapid quenching.

As shown in Fig. 3-2b, the metallic particles (e.g. binary AuNi) on crystalline (i.e. less defective) carbon will only coarsen at high temperature to reduce their surface energy as a thermodynamically favorable process. However, if the carbon contains defects, namely oxygenated carbon, the particles can be uniformly dispersed after three steps.

Step I: Salt decomposition. At high temperature, the salt precursors decompose and form liquid metals on carbon. The high temperature ensures total decomposition of the salt precursors and provides energy for these liquid metals to move around on the carbon surface.

Step II: Particle fusion and fission. The liquid metals actively move around on the substrate. However, growth is hindered by the defective sites present on the carbon support. The particles can undergo particle fission by interaction with O^* on the carbon surface, which promotes the catalytic carbon metabolism reaction [$C + O^* = CO$ (gas)] at high temperature. Also, particle fusion occurs when particles meet and fuse. Catalytically driven particle fission is the key step to form uniformly distributed nanoparticles on the carbon surface, which is in stark contrast to a pure fusion and coalescence mechanism.

Step III: Dynamic steady state. Based on later analysis (Fig. 3-6), fission and fusion of ~10 nm metallic nanoparticles at 2000 K should occur much faster than a 0.1 μs timescale. Therefore, in a 55 ms shock process, it is estimated that the particles can make at least $>10^6$ random steps to ensure uniformity in both size and composition.

The existence of catalytic carbon metabolism during the CTS process is confirmed by in situ molecular beam mass spectra (Fig. 3-3). Enabled by catalytic carbon metabolism, carbon (C), defects (O*) and metals (catalysts) undergo solid-liquid-vapor catalytic reaction, which provides the driving force for particle fission to increase the metal surface area to catalyze the reaction. Particle fission does increase the surface energy of the particles, but the energy loss in the catalytic reaction $C + O^* = CO$ (gas) ($\Delta H = -110.5\ \mathrm{kJ/mol}$) is much higher. Thus, the overall process involving particle fission is energetically favorable. In literature, particle splitting/fission has been proven to occur for supported metallic nanoparticles involving the catalytic reactions (23-26).

Without the supply of fuel (C) and oxidizer (O*), at high temperatures, the metal particles will only coarsen on carbon to minimize their surface energy, which follows conventional high temperature alloying/wetting knowledge.

To verify the effects of supports with more surface-bound defects, we synthesized quinary HEA-NPs (PtFeCoNiCu) on CNFs with and without CO_2 activation (CO_2 activation treatment can create more surface-bound defects), resulting in 5.30 ± 1.31 nm particles on CO_2-activated CNFs and 11.3 ± 2.2 nm particles on CNFs (Fig. 3-4). We achieved further improvements in ultrafine particle sizes and narrow distributions when more catalytically active metal combinations (PtPdIrRhRu HEA-NPs, 3.28 ± 0.81 nm) are employed on identical CO_2-activated CNF supports (Fig. 3-2d and Fig. 3-5). Therefore, the catalytic metabolism-induced particle fission/fusion mechanism for metal alloying at the nanoscale is distinct compared with previously reported alloying methods (1, 3, 7, 16).

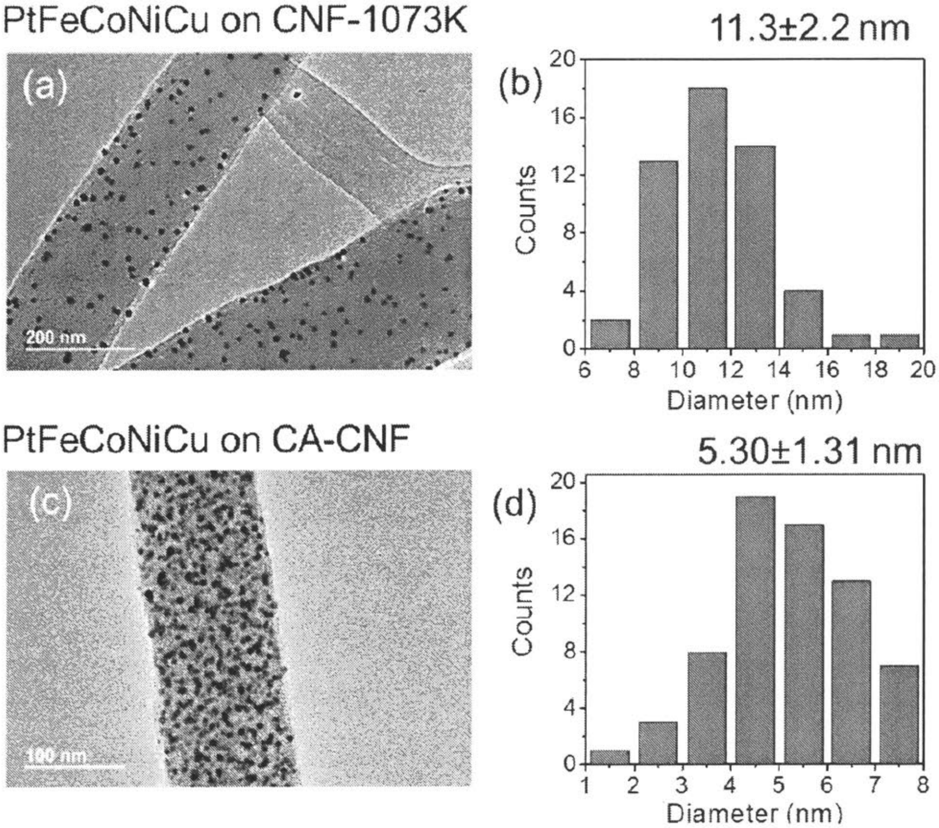

Fig. 3-4. HEA-NPs on CNFs with and without CO_2 activation. (a)-(b) TEM and size distribution of PtFeCoNiCu on CNFs. (c)-(d) TEM and size distribution of PtFeCoNiCu on CO_2-activated CNFs (CA-CNFs).

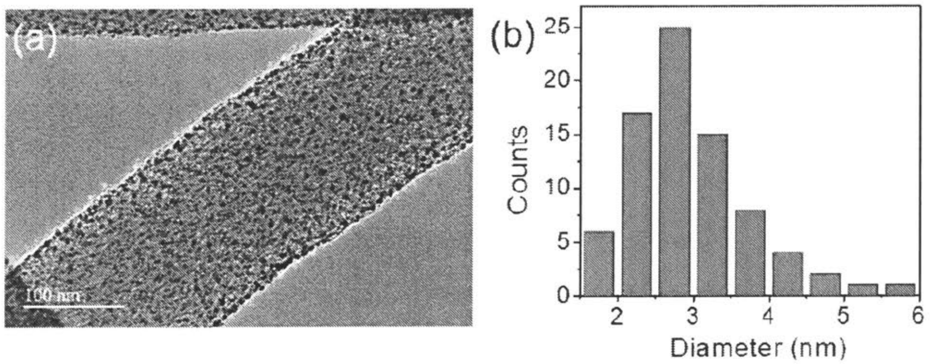

Fig. 3-5. Ultrafine and well-dispersed quinary HEA-NPs (PtPdIrRhRu) formed on CA-CNFs. (a)-(b) TEM image and size distribution of quinary HEA-NPs (PtPdIrRhRu) on CA-CNFs, which shows a narrow size distribution (3.28 nm ± 0.81 nm).

3.2 Kinetics

3.2.1 Timescale analysis

(i) Timescale for catalytically-driven particle fission/fusion

Based on the systematic calculations shown in "*Changing Shapes in the Nanoworld*" (28), fission and fusion of metallic nanoparticles at 800 K should occur at a microsecond timescale (Fig. 3-6a). For a ~10 nm spherical nanoparticle, which contains roughly 30,000 atoms (log(N) ~ 4.48, where N is the number of atoms in the sample), the relaxation time (t_{eq}) is on the order of ~100 μs. It should be noted that the CTS process occurs at a much higher temperature (~2000 K) and thus, the relaxation time should be at least 3-4 orders of magnitude faster than at 800 K. As shown in Fig. 3-6b, the estimated surface diffusivity of metals at 2000 K (1E-4 cm^2/s) is ~3-4 orders of magnitude higher than at 800 K (6E-8 cm^2/s). Therefore, it is expected that the timescale for shape change to occur at 2000 K should be around 0.01-0.1 μs. Note that we used 0.1 μs as the timescale for later analysis.

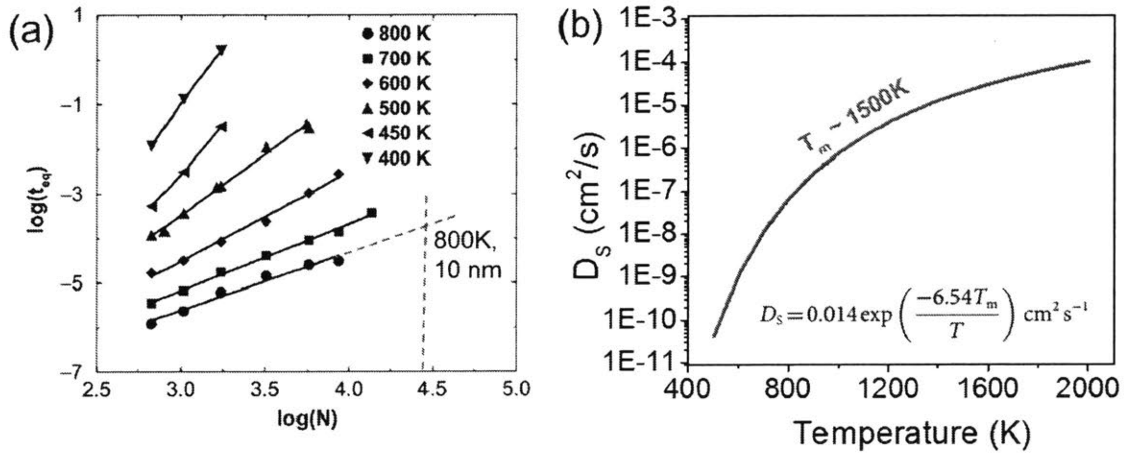

Fig. 3-6. Timescale for catalytically-driven particle fission/fusion. (a) Log-log plot showing relaxation time (t_{eq}) as a function of the crystallite size (N is the number of atoms) at different temperatures (28). (b) Estimation of temperature-dependent surface diffusivity for metals with a melting temperature of ~1500 K. The inset equation is used for estimation, where D_s is the diffusivity, T_m is the melting point, and T is temperature (30).

(ii) Timescale for random diffusion of precursor elements

Note that the size of the salt precursor (and the resultant metal droplets) is in the range of 1-10 μm. For a metal droplet with a size of 1 μm (log(N) = 10.48) or 10 μm (log(N) = 13.48), the timescale for random diffusion is ~$10^{3.8}$ s (~6,300 s) and $10^{7.7}$ s (~50,118,723 s), respectively, based on extrapolations of the relaxation time curve at 800 K. At 2000 K, the timescale of random diffusion would be 3-4 orders of magnitude faster, corresponding to ~10 s or 50,000 s for 1 μm and 10 μm droplets, respectively. Note that this is still a significantly longer amount of time than the 55 ms duration of our CTS synthesis. Therefore, random diffusion of the precursor elements is not the underlying mechanism.

(iii) Timescale for droplet movement across the carbon surface in our fission-fusion process

The liquid metal droplets move by caterpillar-like "peristaltic motion" that involves elongation and shrinkage of each particle to harvest O*, which occurs on a comparable kinetic timescale as the fission and fusion events. Thus, if peristaltic motion takes 0.1 μs (as calculated above) and consequently, the particle moves by a distance of 10 nm (the particle size) in a random direction, then a 55 ms shock duration would correspond to 550,000 random steps. In this case, the mean migration/diffusion distance would be 10 nm × $(550{,}000)^{1/2}$ = 7.4 μm, which is larger than the distance between precursor particles. So it's sufficient to uniformly disperse the 10 nm nanoparticles on the CNFs from the original precursors during the 55 ms shock duration.

3.2.2 Kinetic control over nanoparticle formation

(i) Shock duration

As defects play a key role in the dispersion of the synthesized nanoparticles, prolonged high temperature durations will remove numerous defects and lead to nanoparticle aggregation, which is also confirmed by the experiments. We loaded multiple CNF samples using an identical PtNi precursor solution and exposed the support to a temperature of ~2000 K for 5 ms, 55 ms, 1 s, and 10 s durations. The faster exposure times yield smaller particle sizes (3.51 ± 0.62 nm for 5 ms and 5.01 ± 1.69 nm for 55ms) compared with prolonged shock durations (8.57 ± 1.98 nm for 1s and 13.30 ± 6.98 nm for 10 s) (Fig. 3-7a and b). As the thermal shock duration increases to 10 s, the size of the HEA-NPs increases and the synthesized particles become less uniform; the high-temperature exposure depletes the number of O* present on the CNF support, which inhibits particle fission and corresponding dispersity (Fig. 3-8).

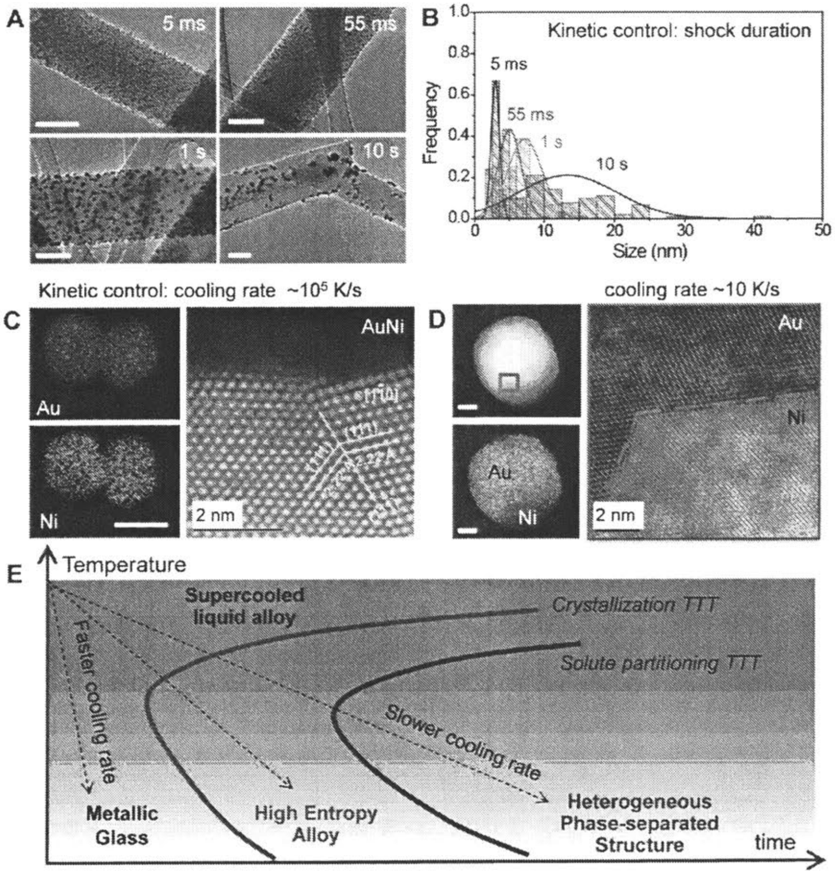

Fig. 3-7. Kinetic control over nanoparticle formation. (a) TEM images displaying the particle size and dispersity at various thermal shock durations (5 ms, 55 ms, 1 s, and 10 s). Scale bars, 100 nm. (b) Particle size distribution of PtNi nanoparticles on CNFs. (c and d) Cooling rate–dependent AuNi nanostructures determined by elemental maps, HAADF, and ABF images. Ultrafast cooling rates (~10^5 K/s) enable the formation of solid-solution nanoparticles, whereas slower rates (~10 K/s) tend to induce phase separation. Scale bar, 10 nm. (e) Time-temperature-transformation (TTT) diagram showing the kinetic formation of metallic glass, HEA, and phase-separated structures, respectively, as a function of cooling rate.

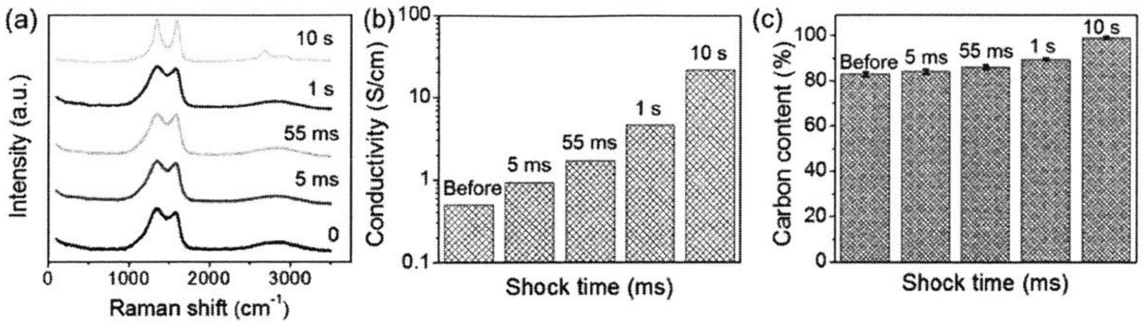

Fig. 3-8. Defect concentrations of CNFs after various shock durations. (a-c) Raman spectra, conductivity measurements and changes in carbon content for CNF-PtNi films after 5 ms, 55 ms, 1 s, and 10 s CTS processes.

(ii) Cooling rate

We investigated the effect of cooling rate by tuning the electrical input parameters (Fig. 2-1b) with Au/Ni and Cu/Co, which are immiscible binary elemental compositions (Fig. 3-7c and d, and Fig. 3-9 to 3-11). Due to differences in lattice parameters and surface energies, these metallic combinations tend to phase-separate according to equilibrium phase diagrams (3, 20, 31). However, through rapid quenching, the high-entropy mixing state of the liquid metals is retained and yields single-phase solid-solution nanoparticles (i.e., HEA-NPs) by avoiding the time-temperature-transformation (TTT) nose (Fig. 3-7e). The AuNi binary alloy formed a solid solution when quenched at both ~10^5 and ~10^3 K/s (Fig. 3-7c and Fig. 3-9b). However, nanoscale phase separation occurred when cooled slowly (~10 K/s), with a clear phase boundary between Au and Ni shown in the annular bright-field (ABF) image (Fig. 3-7d) and HAADF image (Fig. 3-10). For the CuCo binary system, the 10^5 K/s produced a solid solution, but phase separation began at a cooling rate of ~10^3 K/s (Fig. 3-9). Very slow cooling and heating rates (~10 K/s) also alter the dispersion and size distribution of the synthesized nanoparticles, which leads to aggregates and a nonuniform particle dispersion across the CNFs (Fig. 3-11).

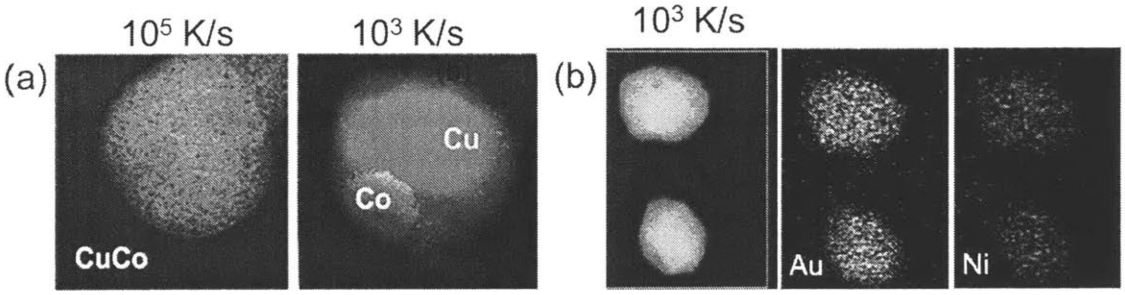
(a)
10^5 K/s
10^3 K/s
CuCo
Cu
Co
(b)
10^3 K/s
Au
Ni

(c)

	10^5 K/s	10^3 K/s	10 K/s
AuNi	Solid solution	Solid solution	Separation
CuCo	Solid solution	Separation	

Fig. 3-9. Rate-dependent non-equilibrium structures for both Cu-Co and Au-Ni systems. (a) CuCo nanoparticles show phase mixing with a ~10^5 K/s cooling rate yet, phase separation occurs when cooled at a rate of ~10^3 K/s. (b) The synthesized AuNi nanoparticles are solid solutions with ~10^5 K/s and ~10^3 K/s cooling rates. Phase separation occurs at a very slow cooling rate of 10 K/s. (c) A table that summarizes the rate-dependent non-equilibrium structures for CuCo and AuNi nanoparticle systems.

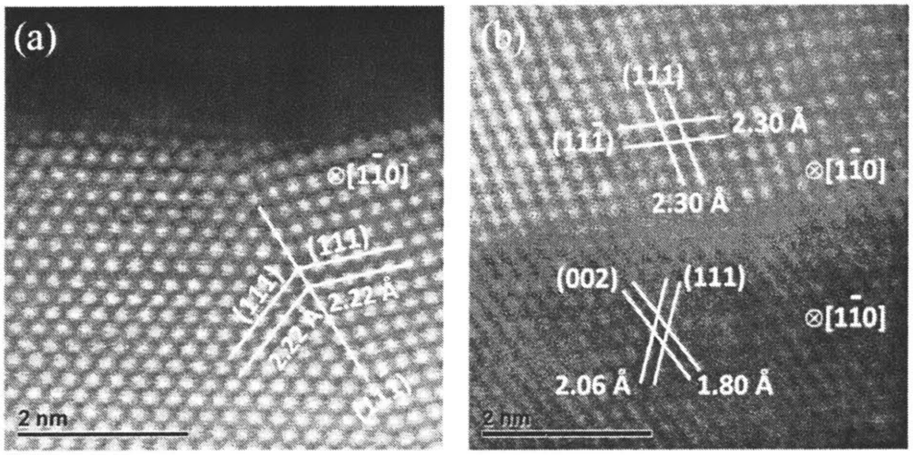
(a)
⊗[$\bar{1}$10]
(111)
(111)
2.22 Å
2.22 Å
(111)
2 nm
(b)
(111)
(11$\bar{1}$)
2.30 Å
2.30 Å
⊗[1$\bar{1}$0]
(002)
(111)
⊗[1$\bar{1}$0]
2.06 Å
1.80 Å
2 nm

Fig. 3-10. Atomic HAADF images of AuNi synthesized with different cooling rates: (a) 10^5 K/s and (b) 10 K/s.

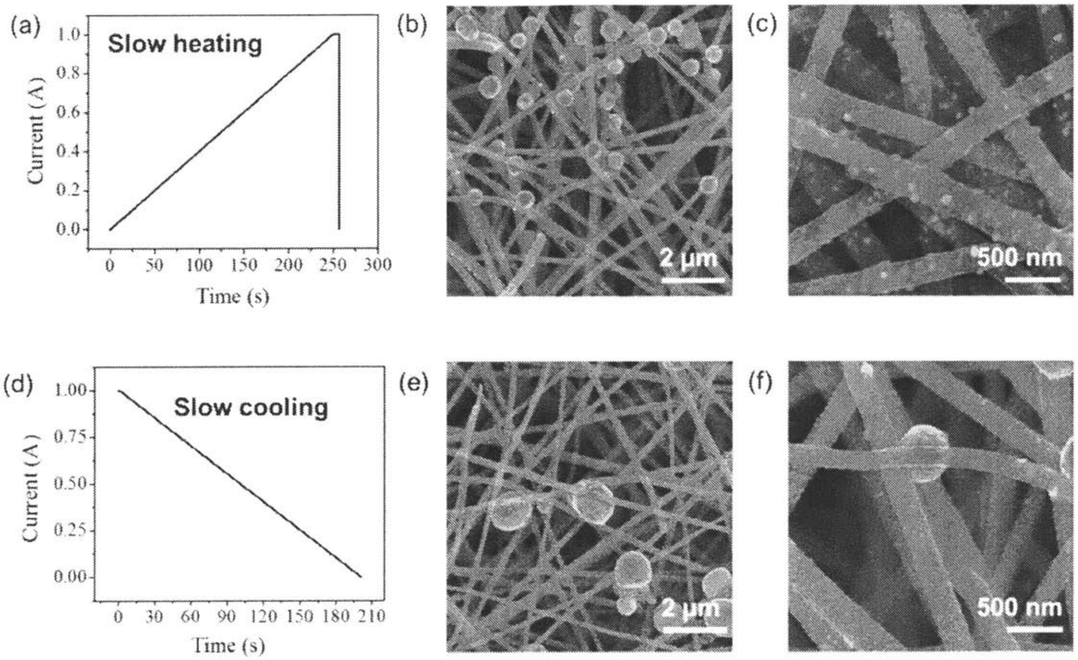

Fig. 3-11. Synthesized nanoparticles by slow heating and cooling rates (control experiments). (a-c) Slow heating profile (10 K/s) and SEM images of the CNF-AuNi system via a slow heating rate. (d-f) Slow cooling profile (10 K/s) and SEM images of the CNF-AuNi using a slow cooling rate.

Our experimental results reveal valuable information about the nucleation and diffusion kinetics of the CTS method. The transformation of a liquid alloy into a single-phase solid solution with a specific elemental composition requires local structural rearrangements but no long-range solute partitioning. The cooling rate (~10^5 K/s) that we achieved by CTS is still slow enough to form crystalline structures. If higher cooling rates are attained with the CTS method, it may be possible to use this route to synthesize metallic glasses. The ~10^5 K/s cooling rate is fast enough to prevent solute partitioning across a distance of ~10 nm, enabling the formation of high-entropy-alloy structures. On the other hand, slower cooling rates (e.g., ~10 K/s) enable solute partitioning to occur through (slow) kinetics, which caused the MMNPs to phase separate into a Janus particle. Both single-phase and phase separated nanoparticles are useful for applications such as catalysis and plasmonic imaging (2, 3, 9, 10). The CTS method has the ability to control phase formation through ramp rates, and the kinetic formation shown in the Time-temperature-transformation (TTT) diagram (Fig. 3-7e) may be quite useful for targeted nanoparticle synthesis.

Chapter 4

Conclusion

The novel mechanism for metal alloying at the nanoscale realized by CTS method provides an excellent platform for nanometallurgical studies. Immiscible elements are alloyed into single-phase nanoparticles on carbon supports with the following features: (i) high-entropy mixing, where multimetallic mixing leads to the creation of solid-solution nanoparticles with maximized configurational mixing entropy; (ii) nonequilibrium processing, where the shock process takes milliseconds to create HEA-NPs by rapid quenching and thus prevents phase separation among immiscible elements by avoiding the nose of the TTT curve (Fig. 3-7e); and (iii) uniform dispersion, where the catalytically driven carbon metabolism at high temperature enables uniform, well-dispersed, and controllably sized nanoparticles (as opposed to particle coarsening).

This synthetic technique also provides (i) generality, (ii) tunability, and (iii) potential scalability. The maximum temperature of the CTS method (2000 to 3000K) is higher than the decomposition temperature of any metal salt, which promotes uniform mixing of nearly any metallic combination (i.e., generality). Precise control over the shock parameters (temperature, duration, and ramp rates) effectively tunes the particle size, dispersity, as well as final structure. The synthesis of a diverse array of nanoparticles with easily tunable processing parameters is ideal for large-scale nanomanufacturing, where a rapid (synthesis in milliseconds) and energy-efficient (immediate heating through an electrical pulse) synthetic procedure could enable high-rate and high-volume production of quality nanoparticles. These CTS capabilities facilitate a new research area for materials discovery and optimization, where the elemental composition and mixing entropy of nanoparticles can be carefully designed and controlled. Further compositional exploration has the potential to transcend research efforts to broad technological applications.

References

1. P.-C. Chen et al., Science 352, 1565–1569 (2016).

2. L. Bu et al., Science 354, 1410–1414 (2016).

3. S. G. Kwon et al., Nat. Mater. 14, 215–223 (2015).

4. M. Takahashi et al., Sci. Adv. 3, e1700101 (2017).

5. X. Huang et al., Science 348, 1230–1234 (2015).

6. G. Chen et al., Science 344, 495–499 (2014).

7. M. R. Buck, J. F. Bondi, R. E. Schaak, Nat. Chem. 4, 37–44 (2011).

8. N. A. Frey, S. Peng, K. Cheng, S. Sun, Chem. Soc. Rev. 38, 2532–2542 (2009).

9. M. B. Cortie, A. M. McDonagh, Chem. Rev. 111, 3713–3735 (2011).

10. K. D. Gilroy, A. Ruditskiy, H.-C. Peng, D. Qin, Y. Xia, Chem. Rev. 116, 10414–10472 (2016).

11. E. Reddington et al., Science 280, 1735–1737 (1998).

12. P. C. Chen et al., J. Am. Chem. Soc. 137, 9167–9173 (2015).

13. P.-C. Chen et al., J. Am. Chem. Soc. 139, 9876–9884 (2017).

14. S. Ranganathan, Curr. Sci. 85, 1404–1406 (2003).

15. J.-W. Yeh et al., Adv. Eng. Mater. 6, 299–303 (2004).

16. B. S. Murty, J.-W. Yeh, S. Ranganathan, High-Entropy Alloys (Butterworth-Heinemann, 2014).

17. Z. Li, K. G. Pradeep, Y. Deng, D. Raabe, C. C. Tasan, Nature 534, 227–230 (2016).

18. Y. F. Ye, Q. Wang, J. Lu, C. T. Liu, Y. Yang, Mater. Today 19, 349–362 (2016).

19. D. C. Hofmann et al., Nature 451, 1085–1089 (2008).

20. D. A. Porter, K. E. Easterling, M. Y. Sherif, Phase Transformations in Metals and Alloys (CRC Press, ed. 3, 2009).

21. L. S. Lobo, S. A. C. Carabineiro, Kinetics and mechanism of catalytic carbon gasification. Fuel 183, 457–469 (2016).

22. N. Eustathopoulos, M. G. Nicholas, B. B. Drevet, Wettability at High Temperatures (Elsevier, 1999), vol. 3.

23. M. Lukas et al., Nat. Commun. 4, 1379 (2013).

24. F. Tao et al., Science 322, 932–934 (2008).

25. M. A. Newton, C. Belver-Coldeira, A. Martínez-Arias, M. Fernández-García, Nat. Mater. 6, 528–532 (2007).

26. F. Tao et al., Science 327, 850–853 (2010).

27. P.-H. Lu et al., arXiv:1802.00207 [physics.app-ph] (1 Feb 2018).

28. N. Combe, P. Jensen, A. Pimpinelli, Phys. Rev. Lett. 85, 110–113 (2000).

29. C. C. Wang et al., Nano Res. 8, 2143–2151 (2015).

30. D.-G. Xie et al., Nat. Mater. 14, 899–903 (2015).

31. D. Wang, Y. Li, J. Am. Chem. Soc. 132, 6280–6281 (2010).

32. D. M. Considine, Chemical and Process Technology Encyclopedia (CRC Press, 1974).

33. L. Xin, H. Yongqiang, J. Husheng, Rare Met. Mater. Eng. 46, 339–343 (2017).

34. P. A. J. Bagot et al., J. Phys. Chem. C 118, 26130–26138 (2014).

35. B. V. I. Chernyshov, I. M. Kisil, Platin. Met. Rev. 37, 136–143 (1993).

36. X. Hu, Y. Ning, L. Chen, Q. Shi, C. Jia, Platin. Met. Rev. 56, 40–46 (2012).